IEEE Access
Multidisciplinary | Rapid Review | Open Access Journal

Received October 30, 2018, accepted November 16, 2018, date of publication November 29, 2018,
date of current version December 27, 2018.

Digital Object Identifier 10.1109/ACCESS.2018.2883869

Multi-Sensor Multi-Floor 3D Localization With Robust Floor Detection

YOU LI[1], (Member, IEEE), ZHOUZHENG GAO[2,3], ZHE HE[1], (Member, IEEE), PENG ZHANG[4], RUIZHI CHEN[4], AND NASER EL-SHEIMY[1]

[1]Department of Geomatics Engineering, University of Calgary, Calgary, AB T2N 1N4, Canada
[2]School of Land Science and Technology, China University of Geosciences Beijing, Beijing 100083, China
[3]German Research Centre for Geosciences (GFZ), 14473 Potsdam, Germany
[4]State Key Laboratory of Surveying, Mapping and Remote Sensing, Wuhan University, Wuhan 430079, China

Corresponding author: Zhouzheng Gao (zhouzhenggao@126.com)

This work was supported in part by the National Natural Science Foundation of China for Young Scientists under Grant 41804027 and in part by the Natural Sciences and Engineering Research Council of Canada.

ABSTRACT Location has become an essential part of the next-generation Internet of Things systems. This paper proposes a multi-sensor-based 3D indoor localization approach. Compared with the existing 3D localization methods, this paper presents a wireless received signal strength (RSS)-profile-based floor-detection approach to enhance RSS-based floor detection. The profile-based floor detection is further integrated with the barometer data to gain more reliable estimations of the height and the barometer bias. Furthermore, the data from inertial sensors, magnetometers, and a barometer are integrated with the RSS data through an extend Kalman filter. The proposed multi-sensor integration algorithm provided more robust and smoother floor detection and 3D localization solutions than the existing methods.

INDEX TERMS Internet of Things, indoor localization, wireless received signal strength, inertial navigation, magnetometer sensor, barometer, 3D, floor detection.

I. INTRODUCTION

The next-generation internet of things (IoT) systems will become increasing dependent on intelligent technologies such as autonomous localization, big data, and intellisense. Accordingly, the location information is becoming an essential part of the IoT systems [1]. The global navigation satellite systems (GNSS) and inertial navigation systems (INS) based outdoor localization systems have achieved great advances over the past decades [2]. In contrast, robust indoor positioning remains an open issue due to factors such as the degradation of GNSS signals in deep indoor areas, the complexity of indoor environments and the diversity in low-cost devices and system deployments [3].

Wireless localization is one of the most widely used indoor localization methods. Although wireless signals such as Bluetooth low energy (BLE) and wireless local area network (WiFi) can be utilized to provide long-term accurate positions that do not drift over time, achieving high-accuracy wireless localization is challenging. The challenges include the dependency on signal availability and geometry [4] and the existence of RSS fluctuations and interferences such as the non-line-of-sight condition [6], reflections [7], multipath [8], and the human body disturbance [9].

To obtain more reliable localization solutions, sensor-based dead-reckoning (DR) has been used as an augmentation to wireless localization [5]. The short-term DR solution can be utilized to bridge the outages of wireless signals, provide smoother solutions when integrated with wireless positioning [10], and aid the profile-based wireless fingerprinting [11] and access point localization and signal-propagation model estimation [30]. Crowdsourcing based on DR data has also been researched [20], [21]. The challenges for low-cost sensor-based DR include the existence of sensor errors [12] and thermal drifts [13], the necessity of initialization [14], the existence of frequent magnetic disturbances [14], and the misalignment angle between the vehicle (e.g., human body) and the device [15].

Due to the complementary characteristics of wireless positioning and DR, their integration has been widely used. Most of the existing indoor localization works are focusing on the two-dimensional (2D) case. That is, the localization activity is restrained in a single floor. However, in the IoT era, numerous devices may be used in various 2D and three-dimensional (3D) scenarios. Thus, the 3D localization technique is needed. A practical approach for 3D indoor localization is to determine the floor in which the device is located and then localize

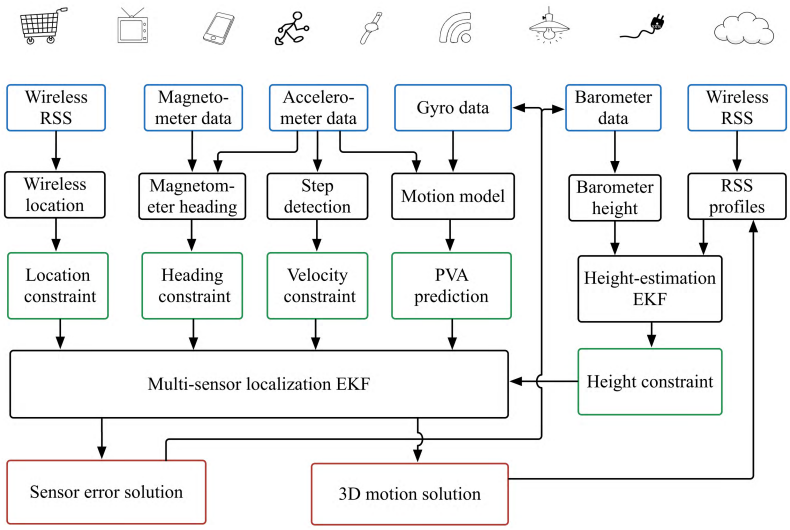

FIGURE 1. Diagram for proposed 3D localization method.

the device within the selected floor. Therefore, accurate floor detection is essential for a robust 3D localization. For floor detection, data from various types of sensors and their combinations have been investigated, such as

- RSS from wireless sensors, e.g., WiFi [16]– [19], BLE [22], and cellular [23]
- Air pressure measured by a barometer [24]– [26]
- Inertial sensors (i.e., gyros and accelerometers) [27]
- The integration of RSS and barometer data [28], [29], [31]
- The integration of RSS and inertial sensor data [32], [33]
- The integration of RSS and the floor plan (i.e., indoor map) [34]
- The integration of barometer data and the floor plan [35]
- The integration of RSS, inertial sensor data, and barometer data [36]
- The integration of RSS, inertial sensor data, and the floor plan [37], [38]
- The integration of RSS, inertial sensor data, and the user position probability map [39].

Meanwhile, various techniques and algorithms have been proposed for floor detection. These techniques include

- Kalman filter [28], [36].
- Particle filter [37], [39], [38].
- The crowdsourcing-based methods [24], [32].
- The simultaneous localization and mapping (SLAM)-based approaches [29], [31], [40].
- Neural Networks [16], [17], [19].
- Least squares [22].
- Fingerprinting [19], [23], [41], [42].
- Centroid [22].
- The clustering methods [25], [31], [42].

In this paper, a multi-sensor 3D localization approach is proposed. Compared to the existing 3D localization methods, the main improvements include

- The existing RSS-based floor-detection methods suffer from performance degradations due to RSS fluctuations and interferences. To alleviate this issue, a RSS profile-based floor-detection method is presented. The RSS-profile is generated with the aid from the sensor-based DR solutions. The profile-based method can provide significantly more reliable floor-detection solutions.
- The profile-based floor detection is further integrated with the barometer data to provide a more robust floor-detection solution. Additionally, the barometer bias is estimated in real time by using the data from wireless and inertial sensors as constraints.
- To mitigate the impact of outliers and enhance the reliability of wireless localization, the data from inertial sensors, magnetometers, and a barometer is integrated with the RSS through an extend Kalman filter (EKF). The proposed algorithm provides significantly more robust and smoother 3D locations than the existing multi-sensor integration methods.

Figure 1 illustrates the diagram for the proposed 3D localization method. The inputs, outputs, and the constraints in the algorithm are highlighted by blue, red, and green boxes, respectively. In this algorithm, the measurements from gyros and accelerometers are used for motion (e.g., position, velocity, and attitude (PVA)) prediction through the INS mechanization. The predicted motion states are further used to construct the system model for the multi-sensor localization EKF.

Meanwhile, the accelerometer data is used for step detection, while the data from magnetometers and accelerometers are utilized for heading determination. The calculated heading and step results are further used to construct the heading

and velocity updates for the EKF. Additionally, the wireless RSS data is used to generate wireless location updates for the EKF. By fusing the motion predictions and location, velocity, and heading updates in the EKF, a 3D location solution can be gained.

Another part in the proposed algorithm is the height-estimation module. In this module, the wireless RSS is combined with the location solution to generate the RSS profiles. The RSS profiles are further integrated with the barometer measurements in the height-estimation EKF to estimate the height. The estimated height is utilized to construct a height constraint for the multi-sensor localization EKF.

This paper is organized as follows. Section II illustrates the multi-sensor-based localization method, Section III describes the height estimation approach, Section IV shows the experimental verification, and Section V draws the conclusions.

II. MULTI-SENSOR LOCALIZATION

This section describes the modules in the multi-sensor integrated localization algorithm. The modules include those for motion prediction and the heading, height, velocity, and position constraints.

A. MOTION PREDICTION

The INS mechanization [43] is used to provide the motion prediction. The gyro-measured angular rates are first used to track the device attitude. The obtained attitude is then used to transform the accelerometer-measured specific forces from the device body frame (i.e., b-frame) to the local-level navigation frame (i.e., n-frame). Afterwards, the gravity vector is added to the n-frame specific force vector to obtain the acceleration vector. Finally, the acceleration is integrated once to determine the velocity and twice to track the position. The continuous-time INS mechanization algorithm in the n-frame is

$$\begin{bmatrix} \dot{\boldsymbol{r}}^n \\ \dot{\boldsymbol{v}}^n \\ \dot{\boldsymbol{C}}_b^n \end{bmatrix} = \begin{bmatrix} \boldsymbol{D}^{-1}\boldsymbol{v}^n \\ \boldsymbol{C}_b^n\boldsymbol{f}^b - [(2\boldsymbol{\omega}_{ie}^n + \boldsymbol{\omega}_{en}^n)\times]\boldsymbol{v}^n + \boldsymbol{g}^n \\ \boldsymbol{C}_b^n[\boldsymbol{\omega}_{ib}^b\times] - [\boldsymbol{\omega}_{in}^n\times]\boldsymbol{C}_b^n \end{bmatrix} \tag{1}$$

where $\boldsymbol{D} = diag(\begin{bmatrix} R_m + h & (R_n + h)cos(l) & -1 \end{bmatrix})$, $\boldsymbol{r}^n = \begin{bmatrix} l & \lambda & h \end{bmatrix}^T$ represents the position vector (latitude, longitude, and height); $\boldsymbol{v}^n = \begin{bmatrix} v_N & v_E & v_D \end{bmatrix}^T$ denotes the velocity vector (north, east, and down velocities); $\boldsymbol{C}_b^n$ is the direction cosine matrix from the b-frame to the n-frame; $\boldsymbol{f}^b$ is the accelerometer measurement vector, and $\boldsymbol{\omega}_{ib}^b$ the gyro measurement vector; $\boldsymbol{\omega}_{ie}^n$ and $\boldsymbol{\omega}_{en}^n$ represent the angular rate of the Earth and that of the n-frame with respect to the e-frame; $\boldsymbol{\omega}_{in}^n$ represent the angular rate of the n-frame with respect to the inertial frame (i.e., i-frame); $\boldsymbol{g}^n$ is the local gravity vector; R_m and R_n are the radius of curvature of meridian and curvature in the prime vertical, respectively, and h is the height. The sign $[\boldsymbol{v}\times]$ denotes the skew-symmetric matrix of $\boldsymbol{v}$, and the sign $diag(\boldsymbol{v})$ indicates the diagonal matrix form of the vector $\boldsymbol{v}$.

B. HEADING CONSTRAINT

The magnetometer data is utilized to compute an absolute heading through the following steps [44]: a) leveling the magnetometer measurements by using the horizontal (i.e., roll and pitch) angles, b) using the leveled magnetometer measurements to calculate the magnetic heading (i.e., the heading angle from the Earth's magnetic north), and c) calculating the true heading (i.e., the heading angle from the Earth's geographic north) by adding a declination angle to the magnetic heading.

The device horizontal angles can be computed by the accelerometer-measured specific forces as

$$\begin{aligned} \phi &= atan2\left(-f_y, -f_z\right) \\ \theta &= atan2\left(f_x, (f_y^2 + f_z^2)^{\frac{1}{2}}\right) \end{aligned} \tag{2}$$

where f_i represents the specific force along the i-th accelerometer axis; ϕ and θ denote the roll and pitch angles, respectively. The sign $atan2()$ is the four-quadrant inverse tangent function.

By following [43], the direction cosine matrix that involves the horizontal angles can be computed as

$$\begin{aligned} \boldsymbol{C}_b^n &= \begin{bmatrix} cos(\theta) & 0 & sin(\theta) \\ 0 & 1 & 0 \\ -sin(\theta) & 0 & cos(\theta) \end{bmatrix} \begin{bmatrix} 1 & 0 & 0 \\ 0 & cos(\phi) & -sin(\phi) \\ 0 & sin(\phi) & cos(\phi) \end{bmatrix} \\ &= \begin{bmatrix} cos(\theta) & sin(\phi)sin(\theta) & cos(\phi)sin(\theta) \\ 0 & cos(\phi) & -sin(\phi) \\ -sin(\theta) & sin(\phi)cos(\theta) & cos(\phi)cos(\theta) \end{bmatrix} \end{aligned} \tag{3}$$

Afterwards, the x-, y-, and z-axis magnetometer readings can be converted into the horizontal magnetic intensities by

$$\begin{bmatrix} m_{H,x} & m_{H,y} \end{bmatrix}^T = \boldsymbol{C}_b^n \begin{bmatrix} m_x & m_y & m_z \end{bmatrix}^T \tag{4}$$

where $\begin{bmatrix} m_{H,x} & m_{H,y} \end{bmatrix}$ is the transformed magnetometer readings in the horizontal plane. The true heading can be computed as

$$\psi = \psi_M + D = -atan2\left(m_{H,y}, m_{H,x}\right) + D \tag{5}$$

where ψ and ψ_M are the true and magnetic headings, respectively. D is the declination angle, which can be obtained from the international geomagnetic reference field (IGRF) model [46].

When the magnetometer-derived heading is available, it can be utilized to build a heading measurement model for the EKF. The heading measurement model can be written as

$$\tilde{\psi} - \hat{\psi} = \delta\psi + n_\psi \tag{6}$$

where $\tilde{\psi}$ is the magnetometer-derived heading, $\hat{\psi}$ is the heading prediction from the motion model, $\delta\psi$ is the heading error to be estimated, and n_ψ is the heading measurement noise.

C. HEIGHT CONSTRAINT

When the height measurement (e.g., by fusing the RSS-profile and barometer data in Section III) is available,

it can be utilized to build a height measurement model for the EKF. The height measurement model can be written as

$$\tilde{h} - \hat{h} = \delta h + n_h \tag{7}$$

where $\tilde{h}$ is the height measurement, $\hat{h}$ is the height prediction from the motion model, δh is the height error to be estimated, and n_h is the height measurement noise.

D. VELOCITY CONSTRAINT

When a step is detected in the pedestrian localization case, the device velocity should be approximately zero. If this is the case, the zero velocity update (ZUPT) can be used as a 3D velocity update for the EKF. The ZUPT measurement model can be described as

$$\begin{bmatrix}0 & 0 & 0\end{bmatrix}^T - \hat{\boldsymbol{v}}^n = \delta \boldsymbol{v}^n + \boldsymbol{n}_v \tag{8}$$

where $\hat{\boldsymbol{v}}^n$ is the 3D velocity prediction from the motion model, $\delta \boldsymbol{v}^n$ is the velocity errors to be estimated, and $\boldsymbol{n}_v$ is the velocity measurement noise vector.

The pedestrian steps are detected by using the the peak-detection method in [47] to process the accelerometer data.

E. LOCATION CONSTRAINT

When the wireless RSS is available, it can be utilized to provide an absolute location update through fingerprinting. Fingerprinting consists of two steps: training and positioning. The training step is conducted to build a database that consists of a set of reference points (RPs) with known coordinates and the RSS from the wireless access points (APs). The Wireless fingerprint at the i-th RP is recorded as

$$\begin{aligned} \boldsymbol{F}_i &= \begin{bmatrix}\boldsymbol{r}_i & \boldsymbol{mac}_i & \boldsymbol{rss}_i\end{bmatrix} \\ \boldsymbol{mac}_i &= \begin{bmatrix}mac_{i,1} & mac_{i,2} & \cdots & mac_{i,M}\end{bmatrix} \\ \boldsymbol{rss}_i &= \begin{bmatrix}rss_{i,1} & rss_{i,2} & \cdots & rss_{i,M}\end{bmatrix} \end{aligned} \tag{9}$$

where $mac_{i,j}$ and $rss_{i,j}$ ($j \in [1, M]$) are the media access control (MAC) address and RSS of the j-th AP at the i-th RP, respectively. $\boldsymbol{r}_i$ is the position of the i-th RP, and M is the number of APs.

The positioning step is implemented to find the closest match between the measured RSS and those stored in the database. To calculate the similarity between the measured RSS vector and the reference RSS vectors in the database, the Euclidean distance between the measured and reference RSS vectors is calculated as

$$e_i = |\boldsymbol{s} - \boldsymbol{l}_i| \tag{10}$$

where $\boldsymbol{s}$ and $\boldsymbol{l}_i$ are the measured RSS vector and the reference RSS at the i-th RP, respectively, and e_i is the Euclidean distance.

The position solution from fingerprinting is used as the EKF location update. The corresponding measurement model is

$$\tilde{\boldsymbol{r}}^n - \hat{\boldsymbol{r}}^n = \delta \boldsymbol{r}^n + \boldsymbol{n}_r \tag{11}$$

where $\tilde{\boldsymbol{r}}^n$ is the position solution from fingerprinting, $\hat{\boldsymbol{r}}^n$ is the 3D position prediction from the motion model, $\delta \boldsymbol{r}^n$ is the position errors to be estimated, and $\boldsymbol{n}_r$ is the position measurement noise vector.

The EKF is adopted to fuse the data from the motion prediction and multiple updates. Refer to [43] for the details about the EKF algorithm.

III. HEIGHT ESTIMATION

This section describes the approach for height estimation. As demonstrated in Figure 1, the data from both the barometer and the RSS-profile is integrated. The following subsections illustrates the methods for height estimation using the barometer data, RSS, and the RSS profile, as well as their integration.

A. BAROMETER HEIGHT

The barometer-measured air pressure can be converted to the barometer height. With the model in [48], the barometer height can be computed as

$$h_b = 44330\left(1.0 - \left(\frac{100p}{p_0}\right)^{\frac{1.0}{5.255}}\right) \tag{12}$$

where h is the barometer height, p and p_0 are the measured air pressure and the sea level reference pressure, respectively. The p_0 value is set at 101325 Pa for calculation.

B. RSS-BASED FLOOR DETECTION

It has been proven that RSS from APs at multiple floors can be utilized for floor detection [16]– [19], [22], [23]. The majority of the existing floor-detection methods are based on the principle of fingerprinting. The fingerprinting-based methods are not dependent on the knowledge of AP locations and path-loss model (PLM) parameters. However, such methods suffer from a heavy computational load and performance degradations when the device is located at a point that does not exist in the fingerprinting database.

In this paper, the geometry for the wireless signals from the APs on each floor is used to weight the probability for each floor. The principle for this method is that if the device is located at a certain floor, the geometry for the wireless signals from the APs on this floor should be stronger than that for the wireless signals from the APs on the other floors. Refer to [45] for details about the geometry of wireless measurements. The dilution of precision (DOP) value is adopted to quantify the geometry of wireless measurements, and thus be used as the score to weight the probability for each floor. The floor that has the smallest positional DOP (PDOP) value will have the highest probability to be the floor where the device is located at.

With the method in [45], the PDOP value for the APs at a certain floor is computed as

$$\chi = \left(\sum_{k=1}^{3} \boldsymbol{D}(k,k)\right)^{\frac{1}{2}}, \quad \boldsymbol{D} = (\boldsymbol{H}^T\boldsymbol{H})^{-1} \tag{13}$$

where χ represents the PDOP value. $\boldsymbol{D}$ represent the matrix that describes the DOP values, and $\boldsymbol{D}(k,k)$ is the k-th diagonal element in $\boldsymbol{D}$. $\boldsymbol{H}$ is the design matrix, which can be computed as

$$\boldsymbol{H} = \begin{bmatrix} \frac{x_u - x_1}{d_1} & \frac{y_u - y_1}{d_1} & \cdots \\ \cdots & \cdots & \\ \frac{x_u - x_i}{d_i} & \frac{y_u - y_i}{d_i} & \\ \cdots & \cdots & \cdots \\ \frac{x_u - x_M}{d_M} & \frac{y_u - y_M}{d_M} & \end{bmatrix} \tag{14}$$

where $\boldsymbol{r}_u = \begin{bmatrix} x_u & y_u \end{bmatrix}$ is the 2D device location vector and $\boldsymbol{r}_i = \begin{bmatrix} x_i & y_i \end{bmatrix}$ is the 2D location vector for the i-th AP. M is the number of APs, and d_i is the geographical distance between the device and the i-th AP. The distance d_i can be calculated by using the method in [49] as

$$d_i = 10^{\frac{rss_i - b_i}{10n_i}} \tag{15}$$

where rss_i is the RSS from the i-th AP, and b_i and n_i are the PLM parameters for the i-th AP. The location x_i and y_i and PLM parameters n_i and b_i for the i-th AP are determined through the least squares by using the measurement model in [49] as

$$\boldsymbol{rss} = -10n_i log_{10}\left(\left((x_i - \boldsymbol{x}_u)^2 + (y_i - \boldsymbol{y}_u)^2\right)^{\frac{1}{2}}\right) + b_i \tag{16}$$

where $\boldsymbol{x}_u = \begin{bmatrix} x_{u,1} \cdots x_{u,j} \cdots x_{u,N} \end{bmatrix}^T$ and $\boldsymbol{y}_u = \begin{bmatrix} y_{u,1} \cdots y_{u,j} \cdots y_{u,N} \end{bmatrix}^T$ are the device locations at multiple RPs, and N is the number of RPs. The state vector to be estimated is $\boldsymbol{x}_i = \begin{bmatrix} x_i & y_i & n_i & b_i \end{bmatrix}^T$. The state vector is estimated through the least-squares method. The design matrix $\boldsymbol{H}_i$ and measurement vector $\boldsymbol{z}_i$ for AP-i location and PP estimation are

$$\boldsymbol{H}_i = \begin{bmatrix} \frac{-10n(x_i - x_{u,1})}{d_1^2 ln10} & \frac{-10n_i(y_i - y_{u,1})}{d_1^2 ln10} & -10log_{10}d_1 & 1 \\ \cdots & \cdots & \cdots & \\ \frac{-10n(x_i - x_{u,j})}{d_j^2 ln10} & \frac{-10n_i(y_i - y_{u,j})}{d_j^2 ln10} & -10log_{10}d_j & 1 \\ \cdots & \cdots & \cdots & \\ \frac{-10n(x_i - x_{u,N})}{d_M^2 ln10} & \frac{-10n_i(y_i - y_{u,N})}{d_M^2 ln10} & -10log_{10}d_M & 1 \end{bmatrix} \tag{17}$$

$$\boldsymbol{z}_i = \begin{bmatrix} rss_1 & \cdots & rss_j & \cdots & rss_N \end{bmatrix}^T \tag{18}$$

Using the least squares, the state vector $\boldsymbol{x}_i$ and the corresponding covariance matrix $\boldsymbol{P}_i$ are estimated by

$$\hat{\boldsymbol{x}}_i = \left(\boldsymbol{H}_i^T \boldsymbol{R}_i^{-1} \boldsymbol{H}_i\right)^{-1} \boldsymbol{H}_i^T \boldsymbol{R}_i^{-1} \boldsymbol{z}_i \tag{19}$$

$$\hat{\boldsymbol{P}}_i = \left(\boldsymbol{H}_i^T \boldsymbol{R}_i^{-1} \boldsymbol{H}_i\right)^{-1} \tag{20}$$

where $\boldsymbol{R}_i = diag(\boldsymbol{n}_{rss})$ and $\boldsymbol{n}_{rss}$ is the RSS measurement noise vector.

To compute the DOP value χ with Equation (13), the 2D device location $\boldsymbol{r}_u = \begin{bmatrix} x_u & y_u \end{bmatrix}^T$ is also required. In this paper, $\boldsymbol{r}_u$ is computed by the weighted average of the AP locations as

$$\boldsymbol{r}_u = \sum_{i=1}^{M} \frac{w_i \boldsymbol{r}_i}{\sum_{i=1}^{M} w_i}, \; w_i = \frac{1}{d_i} \tag{21}$$

C. PROFILE-BASED FLOOR DETECTION

It has been proven in [11] that the short-term DR solution can be combined with the RSS data to generate a RSS-profile, so as to alleviate the position ambiguity issue of wireless positioning. In this paper, the location solution from multi-sensor integration is combined with the RSS data to gain the RSS profile, which is further used for floor detection. The method for generating a RSS profile can be found in [11]. An RSS measurement is appended into the profile only when the device is moving (e.g., when there is a pedestrian step) because the involvement of static data may reduce the diversity of the RSS in the profile. The RSS profile can be written as

$$\boldsymbol{S} = [\boldsymbol{rss}_{i-m+1}, \boldsymbol{rss}_{i-m+2}, \ldots, \boldsymbol{rss}_i] \tag{22}$$

where m represents the number of historical RSS measurements in the RSS profile.

With a RSS profile, the profile-based PDOP value $\boldsymbol{X}$ is calculated by

$$\boldsymbol{X} = \frac{1}{m} \sum_{i=1}^{m} \chi_i \tag{23}$$

The floor that has the smallest $\boldsymbol{X}$ value will have the highest probability to be the floor where the device is located at.

To further enhance the reliability of profile-based floor detection, a blunder detection mechanism is utilized to detect the outliers in the RSS profile. The principle for blunder detection is that the difference between a valid RSS measurement (i.e., not an outlier) in the profile to the mean of all RSS measurements in the profile should be within a threshold value. Therefore, the hypothesis for blunder detection is

$$H_0 : \chi_i - \boldsymbol{X} \leq \alpha_\chi T_\chi \tag{24}$$

where T_χ is the threshold value for blunder detection and α_χ is a scale factor. The T_χ value is described by the standard deviation (STD) value of the RSS measurements in the profile as

$$T_\chi = \left(\frac{1}{m} \sum_{i=1}^{m} (\chi_i - \boldsymbol{X})^2\right)^{\frac{1}{2}} \tag{25}$$

and α_χ is set at a constant such as 3.

If the hypothesis in Equation (24) is rejected, the measurements corresponding to the outliers are removed, and the least squares is used again until all residuals have passed the blunder detection.

D. INFORMATION FUSION FOR HEIGHT ESTIMATION

It can be found from the outcomes in Section IV that the barometer-based approach in Subsection III provided an absolute height; however, it was susceptible to the performance degradation due to the existence of the barometer bias. In contrast, the RSS-profile-based method in Subsection III-C provided a robust floor detection solution but suffered from performance degradation when the user is moving from one floor to another. Therefore, the data from the barometer and RSS are integrated to obtain a more robust height estimation and to calibrate the barometer bias.

An EKF is applied for this integration. The state to be estimated in the height-estimation EKF is $\boldsymbol{x}_h = \begin{bmatrix} h & b_b \end{bmatrix}$, where h is the height and b_b is the barometer bias. In the EKF system model, a pseudo height model is applied. Meanwhile, the barometer bias is modeled as a 1-st order Gauss-Markov process. The EKF system model can be described as

$$\begin{bmatrix} \dot{h} \\ \dot{b_b} \end{bmatrix} = \begin{bmatrix} \boldsymbol{w}_h \\ -\frac{1}{\tau_{b_b}} b_b + \xi_{b_b} \end{bmatrix} \tag{26}$$

where $\boldsymbol{w}_h$ is the system noise for the height, τ_{b_b} and ξ_{b_b} denote for the correlation time and driving noise of the 1-st order Gauss-Markov process, respectively.

When the barometer height is available, it is utilized to build a EKF measurement model as

$$\tilde{h}_b - \hat{h} = \delta h + b_b + n_{h_b} \tag{27}$$

where $\tilde{h}_b$ is the barometer height measurement and n_{h_b} is the corresponding measurement noise.

Additionally, when the RSS-profile-based height is available, it is utilized to build a EKF measurement model as

$$\tilde{h}_p - \hat{h} = \delta h + n_{h_p} \tag{28}$$

where $\tilde{h}_p$ is the RSS-profile-derived height and n_{h_p} is the corresponding measurement noise.

The equations for the height-estimation EKF follows those in [43].

IV. EXPERIMENTAL VERIFICATION

A. TEST DESCRIPTION

The field test was conducted on floors one to four (i.e., F1 to F4) of the energy environment experiential learning (EEEL) building at the University of Calgary. The EEEL building is a modern office building that have complex indoor environments, including both line-of-sight and non-line-of-sight areas, as well as open areas and corridors. The size of each floor at this building was 120 m by 40 m. The test data was collected by using a Samsung S4 Android smartphone, which was equipped with gyro, accelerometer, and magnetometer triads, a barometer, a WiFi receiver, and a GPS receiver. The sampling rates were set at 20 Hz for for gyros, accelerometers, and magnetometers, 1 Hz for the barometer, 0.5 Hz for WiFi, and 0.1 Hz for GPS.

To test the algorithms, the tester held the smartphone and walked along the path in Figure 2. The sequence of user motion was as follows: entered the building from the southwest entrance at F1 -> walked at F1 -> walked up the stairs -> walked at F2 -> walked up the stairs -> walked at F3 -> walked up the stairs -> walked at F4 -> moved down in an elevator -> walked at F3 -> moved down in an elevator -> walked at F2 -> moved down in an elevator -> walked at F1 -> exited the building from the southwest entrance at F1. The sensor measurements during the test are illustrated in the next subsection. The reference trajectories were generated by taking a Lenovo Phab 2 Pro smartphone to collect red-green-blue-depth (RGB-D) images and generate SLAM solutions.

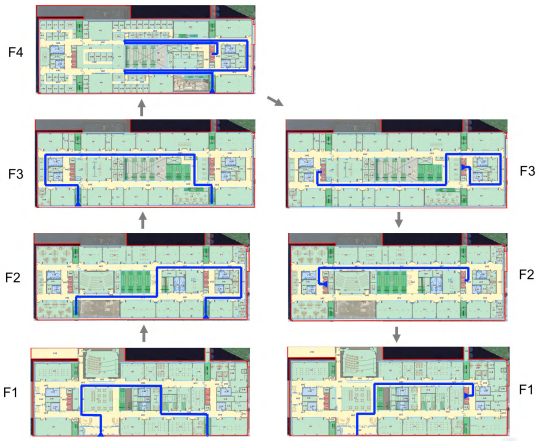

FIGURE 2. Test trajectory and corresponding floor plan.

B. SENSOR MEASUREMENTS AND LOCALIZATION FEATURES

To demonstrate the sensor measurements during the test time period, Figures 3, 4, and 5 show the gyro and accelerometer signals, the magnetometer and barometer measurements, and the WiFi RSS data, respectively. The right subfigures in Figures 3 and 4 are the zoomed-in views of the corresponding left subfigures. The four subfigures in Figure 5 represent the RSS from the APs at the four floors. Eight APs were selected at each floor. It can be seen that the gyro data indicated the straight-walking and turning motions, while the accelerometer data can be utilized to detect the static and moving time periods. Meanwhile, both the barometer and RSS data reflected the changes of height. The former directly reflected the absolute height, while the latter had changes in RSS from APs at each floor when the user moved from one floor to another.

Figure 6 (a) demonstrates the magnetometer-derived heading angles that were computed through the method in Subsection II-B. The time series of magnetometer-derived heading fitted with the reference in the long term but suffered from noises and interferences. Figure 6 (b) shows the height that was calculated by using the barometer data. There was a systematic difference between the barometer height and the corresponding reference.

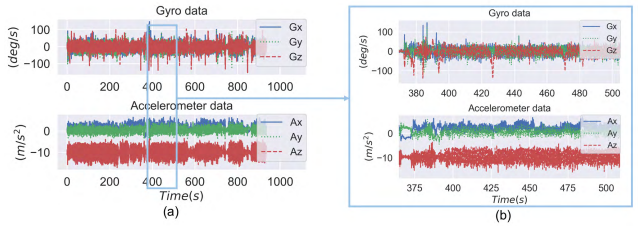

FIGURE 3. Gyro and accelerometer signals.

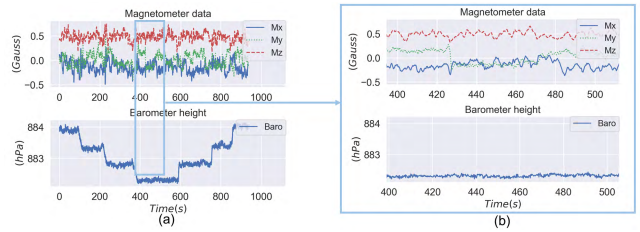

FIGURE 4. Magnetometer and barometer signals.

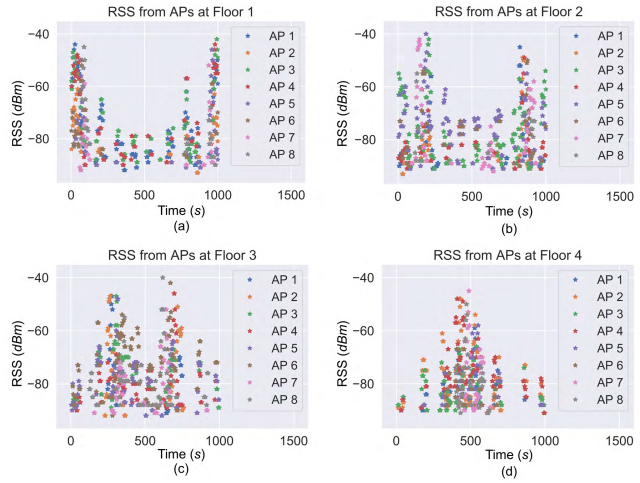

FIGURE 5. WiFi RSS from APs at each floor.

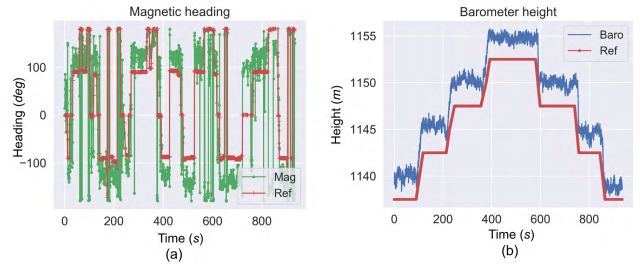

FIGURE 6. Magnetometer-derived heading (a) and barometer-derived height (b).

Figure 7 (a) shows the 2D location solution that was calculated by using the INS mechanization and the ZUPT updates. The solution visualized the trajectory for testing but had increasing drifts over time. Figure 8 illustrates the results of using the accelerometer-measured specific forces to detect

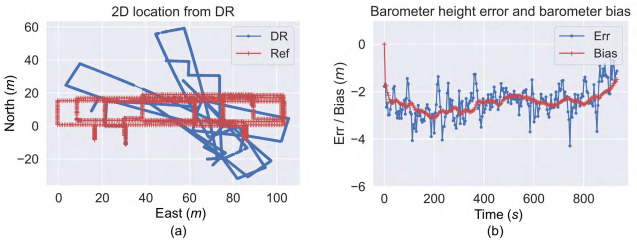

FIGURE 7. 2D DR position (a) and estimated barometer bias (b).

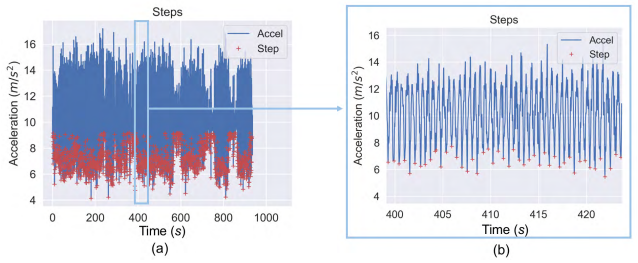

FIGURE 8. Steps detected by using accelerometer measurements.

the pedestrian steps. The blue line denotes the norm values of accelerometer measurements and the red dots show the detected steps.

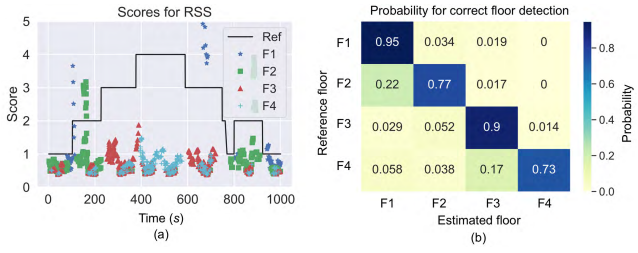

FIGURE 9. RSS-based floor detection solution.

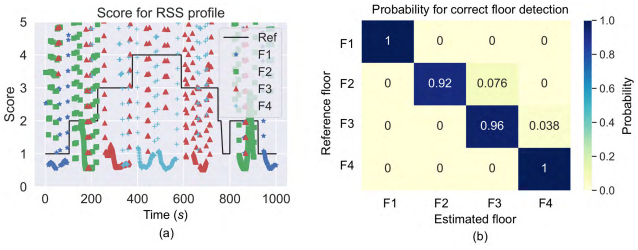

FIGURE 10. RSS profile-based floor detection solution.

C. FLOOR DETECTION RESULTS

Figures 9 and 10 illustrate the floor-detection solutions by using the methods in Subsections III-B and III-C, respectively. The black lines in the left subfigures illustrate the reference floor number, while the blue, green, red, and cyan markers in the right subfigures are the floor-detection scores (i.e., PDOP values for the RSS-based method and the profile-based PDOP values for the profile-based method) for

floors one to four, respectively. When using the RSS-based floor-detection method, the floor-detection scores for adjacent floors were close to one another during several time periods (e.g., those around 200 s and 650 s). Accordingly, 22 % of the F2 solutions were falsely detected to be F1, and 17 % of the F4 solutions were flasely detected to be F3.

With the profile-based method, the differences between the floor-detection scores for adjacent floors had been enlarged significantly. As a result, the false detection rates had been reduced from 5 %, 23 %, 10 %, and 27 % to 0 %, 8 %, 4 %, and 0 % for F1, F2, F3, and F4, respectively.

Figure 7 (b) demonstrates the barometer bias solution that was estimated by using the EKF in Subsection III-D. The blue dots show the difference between the barometer height and the height estimate from the EKF, while the red line illustrates the real-time estimated barometer bias.

D. 3D LOCALIZATION SOLUTIONS

Figure 11 (a) illustrates the RSS fingerprinting solution by using the RSS-based method for floor detection and then using the database at the estimated floor for positioning (i.e., the WiFi-FD strategy). In contrast, Figure 11 (b) demonstrates the RSS fingerprinting solution by using the profile-based method for floor detection and then using the database at the estimated floor for positioning (i.e., the WiFi-PFD strategy). The profile-based floor-detection approach had significantly reduced the probability of large position errors (i.e., "jumps in the position solution") that were caused by a false floor detection but had not eliminated them. Therefore, data from other sources were needed to further enhance the 3D localization solution.

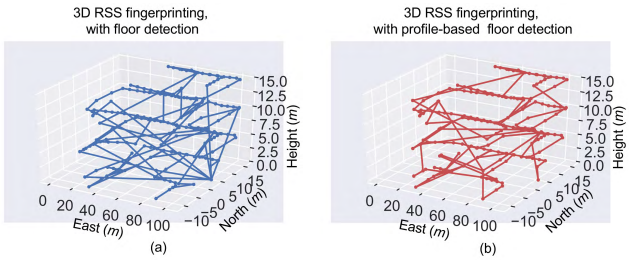

FIGURE 11. RSS-based localization solutions.

Figure 12 (a) shows the 3D localization solution by integrating the solution in Figure 11 (a) with the data from inertial sensors, magnetometers, and the barometer by using the multi-sensor localization EKF in Section II (i.e., the Sensor/WiFi-FD strategy). The method used has a similar principle to the existing works. It can be seen that the large location errors had been reduced after integration with the sensor data. Figure 12 (b) shows the 3D localization solution by integrating the solution in 11 (b) with the sensor data (i.e., the proposed multi-sensor system (MSS) strategy). The MSS strategy provided a smoother 3D location solution than the Sensor/WiFi-FD strategy.

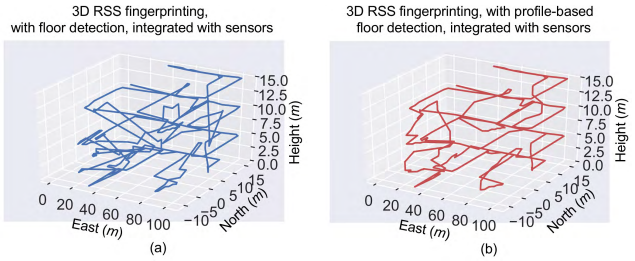

FIGURE 12. Multi-sensor-based localization solutions.

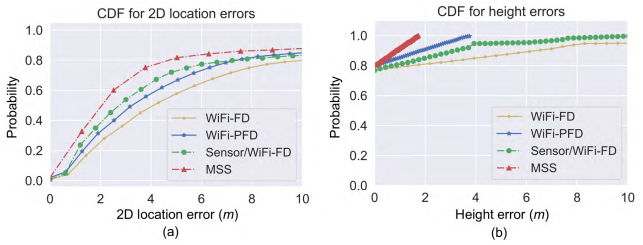

FIGURE 13. CDF of location errors.

Figure 13 illustrates the cumulative distribution function (CDF) of the location errors by using the strategies WiFi-FD, WiFi-PFD, Sensor/WiFi-FD, and MSS. The subfigures (a) and (b) show the error CDF of the 2D horizontal location errors and the 1D height errors, respectively. Meanwhile, Tables 1 and 2 demonstrate the statistics of the 2D horizontal location errors and the 1D height errors, respectively. The error statistics include the STD, mean, root mean square (RMS), the error within which the probability is 80 % (i.e., the 80 % error), and the error within which the probability is 95 % (i.e., the 95 % error).

TABLE 1. Statistics of 2D location errors.

Strategy	STD (m)	Mean (m)	RMS (m)	80% (m)	95% (m)
WiFi-FD	2.8	5.7	7.6	10.1	28.9
WiFi-PFD	2.2	3.6	5.1	7.4	21.0
Sensor/WiFi-FD	1.9	2.7	3.9	7.2	17.8
MSS	1.5	2.1	2.6	4.5	11.8

TABLE 2. Statistics of height errors.

Strategy	STD (m)	Mean (m)	RMS (m)	80% (m)	95% (m)
WiFi-FD	1.2	1.8	2.1	1.4	10.2
WiFi-PFD	0.4	0.9	1.0	1.1	2.7
Sensor/WiFi-FD	0.6	0.6	0.7	0.9	5.1
MSS	0.3	0.4	0.4	0.6	1.3

When the profile-based floor-detection method was applied, the 2D location error RMS value was reduced from 7.6 m in the WiFi-FD strategy to 5.1 m in the WiFi-PFD strategy, with an accuracy improvement of 31.6 %. This outcome indicates the necessity of a robust floor-detection solution on accurate wireless fingerprinting. Meanwhile, when integrated with the sensor data, the 2D location error RMS value

was reduced from 7.8 m in the WiFi-FD strategy to 3.9 m in the Sensor/WiFi-FD strategy, with an accuracy improvement of 48.7 %. When using the MSS strategy, the RMS of 2D location errors were further reduced to 2.6 m, with an accuracy improvement of 33.3 % compared to the Sensor/WiFi-FD strategy.

For the height solution, the WiFi-FD strategy suffered from an error RMS of 2.1 m, which was reduced to 1.0 m and 0.7 m when the WiFi-PFD and Sensor/WiFi-FD strategies were utilized, respectively. These results show the effectiveness of the profile-based method and the integration of sensors on height estimation. Furthermore, the MSS strategy reduced the height error RMS to 0.4 m, with an accuracy improvement of 42.9 % compared to the Sensor/WiFi-FD strategy.

V. CONCLUSION

This paper has proposed a multi-sensor-based three-dimensional (3D) localization approach by integrating the wireless received signal strength (RSS) and the data from inertial sensors, magnetometers, and a barometer. Compared to the RSS-based floor-detection method, the proposed profile-based method improved the floor detection accuracy from 83.8 % to 97.0 %. When using the floor-detection results to aid the RSS-based fingerprinting, the root mean square (RMS) values of the two-dimensional (2D) location errors and the height errors were reduced from 7.6 m and 2.1 m to 5.1 and 1.0 m, respectively, with accuracy improvements of 31.6 % and 52.4 %. Compared to the ordinary multi-sensor integration method, the proposed algorithm further reduced the RMS values of the 2D location errors and the height errors from 3.9 m and 0.7 m to 2.6 and 0.4 m, respectively, with accuracy improvements of 33.3 % and 42.9 %. These outcomes have indicated the effectiveness of the proposed method on floor detection and 3D indoor localization.

REFERENCES

[1] Y. Cao *et al.*, "A trajectory-driven opportunistic routing protocol for VCPS," *IEEE Trans. Aerosp. Electron. Syst.*, to be published, doi: 10.1109/TAES.2018.2826201.

[2] Y. Wang, X. Zhao, C. Pang, B. Feng, and L. Zhang, "The influence of attitude dilution of precision on the observable degree and observability analysis with different numbers of visible satellites in a multi-antenna GNSS/INS attitude determination system," *IEEE Access*, vol. 6, pp. 22156–22164, Apr. 2018.

[3] Y. Zhuang *et al.*, "A survey of positioning systems using visible LED lights," *IEEE Commun. Surveys Tuts.*, vol. 20, no. 3, pp. 1963–1988, 3rd Quart., 2018.

[4] Y. Cheng, X. Wang, M. Morelande, and B. Moran, "Information geometry of target tracking sensor networks," *Inf. Fusion*, vol. 14, no. 3, pp. 311–326, Jul. 2013.

[5] H. Lan, C. Yu, Y. Zhuang, Y. Li, and N. El-Sheimy, "A novel Kalman filter with state constraint approach for the integration of multiple pedestrian navigation systems," *Micromachines*, vol. 15, no. 6, pp. 926–952, Jul. 2015.

[6] Z. Xiao, H. Wen, A. Markham, N. Trigoni, P. Blunsom, and J. Frolik, "Non-line-of-sight identification and mitigation using received signal strength," *IEEE Trans. Wireless Commun.*, vol. 14, no. 3, pp. 1689–1702, Mar. 2015.

[7] L. Liu and H. Liu, "Joint estimation of DOA and TDOA of multiple reflections in mobile communications," *IEEE Access*, vol. 4, pp. 3815–3823, Jun. 2016.

[8] Y. Ma, B. Wang, S. Pei, Y. Zhang, S. Zhang, and J. Yu, "An indoor localization method based on AOA and PDOA using virtual stations in multipath and NLOS environments for passive UHF RFID," *IEEE Access*, vol. 6, pp. 31772–31782, May 2018.

[9] S. Schmitt, S. Adler, and M. Kyas, "The effects of human body shadowing in RF-based indoor localization," in *Proc. Int. Conf. Indoor Positioning Indoor Navigat. (IPIN)*, Busan, South Korea, Oct. 2014, pp. 307–313.

[10] Y. Zhuang, Y. Li, L. Qi, H. Lan, N. El-Sheimy, and J. Yang, "A two-filter integration of MEMS sensors and WiFi fingerprinting for indoor positioning," *IEEE Sensors J.*, vol. 16, no. 13, pp. 5125–5126, Jul. 2016.

[11] Y. Li, Y. Zhuang, H. Lan, X. Niu, and N. El-Sheimy, "A profile-matching method for wireless positioning," *IEEE Commun. Lett.*, vol. 20, no. 12, pp. 2514–2517, Dec. 2016.

[12] Y. Li, J. Georgy, X. Niu, Q. Li, and N. El-Sheimy, "Autonomous calibration of MEMS gyros in consumer portable devices," *IEEE Sensors J.*, vol. 15, no. 7, pp. 4062–4072, Jul. 2015.

[13] X. Niu, Y. Li, H. Zhang, Q. Wang, and Y. Ban, "Fast thermal calibration of low-grade inertial sensors and inertial measurement units," *Sensors*, vol. 13, no. 1, pp. 12192–12217, Sep. 2013.

[14] Y. Li, Y. Zhuang, H. Lan, P. Zhang, X. Niu, and N. El-Sheimy, "Self-contained indoor pedestrian navigation using smartphone sensors and magnetic features," *IEEE Sensors J.*, vol. 16, no. 19, pp. 7173–7182, Oct. 2016.

[15] L. Pei, D. Liu, D. Zou, R. L. F. Choy, Y. Chen, and Z. He, "Optimal heading estimation based multidimensional particle filter for pedestrian indoor positioning," *IEEE Access*, vol. 6, pp. 49705–49720, Aug. 2018.

[16] R. Elbakly, H. Aly, and M. Youssef, "TrueStory: Accurate and robust RF-based floor estimation for challenging indoor environments," *IEEE Sensors J.*, vol. 18, no. 24, pp. 10115–10124, Dec. 2018, doi: 10.1109/JSEN.2018.2872827.

[17] R. Campos, L. Lovisolo, and M. Campos, "Wi-Fi multi-floor indoor positioning considering architectural aspects and controlled computational complexity," *Expert Syst. Appl.*, vol. 41, no. 14, pp. 6211–6223, Oct. 2014.

[18] I. Alshami, N. Ahmad, and S. Sahibuddin, "A light WLAN radio map for floor detection in multi-floor environment localization," in *Proc. 9th Malaysian Softw. Eng. Conf. (MySEC)*, Kuala Lumpur, Malaysia, Dec. 2015, pp. 135–139.

[19] K. Kim *et al.*, "Large-scale location-aware services in access: Hierarchical building/floor classification and location estimation using Wi-Fi fingerprinting based on deep neural networks," in *Proc. Int. Workshop Fiber Opt. Access Netw. (FOAN)*, Munich, Germany, Nov. 2017, pp. 1–5.

[20] L. Pei, M. Zhang, D. Zou, R. Chen, and T. Chen, "A survey of crowd sensing opportunistic signals for indoor localization," *Mobile Inf. Syst.*, vol. 2016, no. 1, pp. 1–16, Apr. 2016.

[21] P. Zhang, Q. Zhao, Y. Li, X. Niu, Y. Zhuang, and J. Liu, "Collaborative WiFi fingerprinting using sensor-based navigation on smartphones," *Sensors*, vol. 15, no. 7, pp. 17534–17557, Jul. 2015.

[22] E. Lohan, J. Talvitie, P. Silva, H. Nurminen, S. Ali-Loytty, and R. Piche, "Received signal strength models for WLAN and BLE-based indoor positioning in multi-floor buildings," in *Proc. Int. Conf. Location GNSS (ICL-GNSS)*, Gothenburg, Sweden, 2015, pp. 1–6.

[23] M. Luckner and R. Gorak, "Comparison of floor detection approaches for suburban area," in *Intelligent Information and Database Systems* (Lecture Notes in Computer Science), vol. 9622. Mar. 2016, pp. 782–791.

[24] H. Ye, T. Gu, X. Tao, and J. Lu, "B-Loc: Scalable floor localization using barometer on smartphone," in *Proc. IEEE 11th Int. Conf. Mobile Ad Hoc Sensor Syst. (MASS)*, Oct. 2014, pp. 127–135.

[25] C. Luo, H. Hong, M. C. Chan, J. Li, X. Zhang, and Z. Ming, "MPiLoc: Self-calibrating multi-floor indoor localization exploiting participatory sensing," *IEEE Trans. Mobile Comput.*, vol. 17, no. 1, pp. 141–154, Jan. 2018.

[26] M. Won, A. Mishra, and S. Son, "HybridBaro: Mining driving routes using barometer sensor of smartphone," *IEEE Sensors J.*, vol. 17, no. 19, pp. 6397–6408, Oct. 2017.

[27] C. Ascher, C. Kessler, R. Weis, and G. F. Trommer, "Multi-floor map matching in indoor environments for mobile platforms," in *Proc. Int. Conf. Indoor Positioning Indoor Navigat. (IPIN)*, Nov. 2012, pp. 1–8.

[28] F. Haque, V. Dehghanian, A. Fapojuwo, and J. Nielsen, "Wi-Fi RSS and MEMS barometer sensor fusion framework for floor localization," *IEEE Sensors J.*, to be published, doi: 10.1109/JSEN.2018.2852494.

[29] H. Wang, A. Szabo, J. Bamberger, and U. D. Hanebeck, "Simultaneous multi-information fusion and parameter estimation for robust 3-D indoor positioning systems," in *Proc. IEEE Int. Conf. Multisensor Fusion Integr. Intell. Syst. (MFI)*, Aug. 2008, pp. 445–450.
[30] Y. Zhuang, Y. Li, H. Lan, Z. Syed, and N. El-Sheimy, "Wireless access point localization using nonlinear least squares and multi-level quality control," *IEEE Wireless Commun. Lett.*, vol. 4, no. 6, pp. 693–696, Dec. 2015.
[31] X. Shen, Y. Chen, J. Zhang, L. Wang, G. Dai, and T. He, "BarFi: Barometer-aided Wi-Fi floor localization using crowdsourcing," in *Proc. IEEE Int. Conf. Mobile Ad Hoc Sensor Syst.*, Dallas, TX, USA, Oct. 2015, pp. 416–424.
[32] H. Ye, T. Gu, X. Tao, and J. Lu, "F-Loc: Floor localization via crowdsourcing," in *Proc. IEEE Int. Conf. Parallel Distrib. Syst. (ICPADS)*, Hsinchu, Taiwan, Dec. 2014, pp. 47–54.
[33] K. Ramana, N. Jianwei, M. Aziz, and M. Umair, "A robust multi-cue blending-based approach for floor detection," in *Proc. Int. Bhurban Conf. Appl. Sci. Technol. (IBCAST)*, Islamabad, Pakistan, Jan. 2016, pp. 647–653.
[34] J. Shi and Y. Shin, "A low-complexity floor determination method based on WiFi for multi-floor buildings," in *Proc. Int. Conf. Telecommun.*, Jun. 2013, pp. 129–134.
[35] H. Wang, H. Lenz, A. Szabo, U. Hanebeck, and J. Bamberger, "Fusion of barometric sensors, WLAN signals and building information for 3-D indoor/campus localization," in *Proc. Int. Conf. Multisensor Fusion Integr. Intell. Syst.*, Sep. 2006, pp. 426–432.
[36] M. Zhou, B. Wang, Z. Tian, J. Wang, and Q. Zhang, "A case study of cross-floor localization system using hybrid wireless sensing," in *Proc. IEEE Global Commun. Conf.*, Singapore, Dec. 2017, pp. 1–6.
[37] C. Lo, T. Chiang, T. Lee, L. Chen, and Y. Tseng, "Wireless location tracking by a sensor-assisted particle filter and floor plans in a 2.5-D space," in *Proc. IEEE Wireless Commun. Netw. Conf. (WCNC)*, Barcelona, Spain, 2018, pp. 1–6.
[38] W. Jaworski, P. Wilk, P. Zborowski, W. Chmielowiec, A. Y. Lee, and A. Kumar, "Real-time 3D indoor localization," in *Proc. Int. Conf. Indoor Positioning Indoor Navigat. (IPIN)*, Sapporo, Japan, 2017, pp. 1–8.
[39] J. Herrera, P. Ploger, A. Hinkenjann, J. Maiero, M. Flores, and A. Ramos, "Pedestrian indoor positioning using smartphone multi-sensing, radio beacons, user positions probability map and IndoorOSM floor plan representation," in *Proc. Int. Conf. Indoor Positioning Indoor Navigat. (IPIN)*, Busan, South Korea, 2014, pp. 636–645.
[40] A. Ozkil, Z. Fan, J. Xiao, S. Dawids, J. Kristensen, and K. Christensen, "Mapping of multi-floor buildings: A barometric approach," in *Proc. IEEE/RSJ Int. Conf. Intell. Robots Syst.*, San Francisco, CA, USA, Sep. 2011, pp. 847–852.
[41] L. Sun, Z. Zheng, T. He, and F. Li, "Multifloor Wi-Fi localization system with floor identification," *Int. J. Distrib. Sensor Netw.*, vol. 11, no. 7, pp. 1–8, Jul. 2015.
[42] A. Razavi, M. Valkama, and E. Lohan, "K-means fingerprint clustering for low-complexity floor estimation in indoor mobile localization," in *Proc. IEEE Globecom Workshops (GC Wkshps)*, San Diego, CA, USA, Dec. 2015, pp. 1–7.
[43] E. Shin, "Estimation techniques for low-cost inertial navigation," Dept. Geomatics Eng., Univ. Calgary, Calgary, AB, Canada, Tech. Rep. UCGE-20219, 2005.
[44] R. Zhang, F. Höflinger, and L. Reindl, "Inertial sensor based indoor localization and monitoring system for emergency responders," *IEEE Sensors J.*, vol. 13, no. 2, pp. 838–848, Feb. 2013.
[45] R. Langley, "Dilution of precision," *GPS World*, vol. 10, no. 5, pp. 52–59, May 1999.
[46] A. Chambodut, "Geomagnetic field, IGRF," in *Encyclopedia of Solid Earth Geophysics*. Dordrecht, The Netherlands: Springer, 2011, doi: 10.1007/978-90-481-8702-7_111.
[47] R. Harle, "A survey of indoor inertial positioning systems for pedestrians," *IEEE Commun. Surveys Tuts.*, vol. 15, no. 3, pp. 1281–1293, 3rd Quart., 2013.
[48] K. Sankaran, M. Zhu, X. Guo, A. Ananda, L. Chan, and L. Peh, "Using mobile phone barometer for low-power transportation context detection," in *Proc. ACM Conf. Embedded Netw. Sensor Syst.*, Memphis, TN, USA, Nov. 2014, pp. 191–205.
[49] Y. Zhuang, Y. Li, H. Lan, Z. Syed, and N. El-Sheimy, "Smartphone-based WiFi access point localisation and propagation parameter estimation using crowdsourcing," *Electron. Lett.*, vol. 51, no. 17, pp. 1380–1382, Aug. 2015.

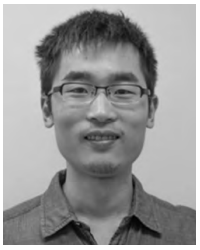

YOU LI (M'16) received the B.Eng. degree from the China University of Geosciences, Beijing, in 2009, the Ph.D. degree from the Department of Geomatics Engineering, University of Calgary, Canada, and the Ph.D. degree from the GNSS Research Center, Wuhan University, China, in 2016. He is a Senior Researcher at the University of Calgary. He was the R&D Lead at Appropolis Inc., the Lead Scientist of EZRoad Ltd., the Algorithm Designer at InvenSense Inc., and the Software Algorithm Engineer at Trusted Positioning Inc. He has co-authored over 50 academic papers, 20 Chinese patents, 3 U.S. patents, and 1 European patent filed or pending. His research interests include mobile multi-sensor system-based positioning, localization, navigation technologies, and their applications in IoT and location-based service applications. Also, he has won a golden medal in the EvAAL Competition and three best paper awards from IEEE, ION, or ISPRS conferences.

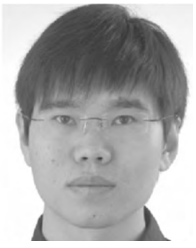

ZHOUZHENG GAO received the bachelor's and master's degrees from the China University of Geosciences Beijing, China, in 2008 and 2012, respectively, and the Ph.D. degree from the School of Geodesy and Geomatics, Wuhan University, in 2016. During 2014 and 2017, he was with the German Research Center for Geosciences (GFZ), Potsdam, Germany, as a Visiting Scholar from 2014 to 2016 and Post-Doctor from 2016 to 2017, respectively. He is currently a Researcher with the School of Land Science and Technology, China University of Geosciences Beijing. To date, he has one authorized software copyright and published 17 papers. His current research interests include GNSS precise positioning algorithms (PPP and RTK), GNSS/INS integration, multi-sensor integration, multi-constellation GNSS real-time positioning, and the application of multi-GNSS/multi-sensor integration.

ZHE HE received the B.S. and M.S. degrees in navigation guidance and control from Shanghai Jiao Tong University, and the Ph.D. degree in geomatics engineering from the University of Calgary, Canada. He was a Post-Doctoral Fellow at the Position, Location And Navigation (PLAN) Group, Department of Geomatics Engineering, University of Calgary, and he is with an IoT company in Calgary. His research interests are statistical estimation theory applied to GNSS, inertial and integrated navigation systems, and low-power wide area network LBS systems.

PENG ZHANG was born in Shiyan, China, in 1988. He received the B.Eng. (Hons.) and Ph.D. degrees in geodesy and surveying engineering from Wuhan University, Wuhan, China, in 2010 and 2016, respectively. From 2016 to 2018, he was an Assistant Researcher with the State Key Laboratory of Information Engineering in Surveying, Mapping and Remote Sensing (LIESMARS), Wuhan University, where he is currently an Associate Researcher. His research interests include indoor navigation, pedestrian navigation, wearable devices, and biosensors.

RUIZHI CHEN is the Director of the State Key Laboratory of Information Engineering in Surveying, Mapping and Remote Sensing, Wuhan University. He used to work as an Endowed Chair and Professor in Texas A&M University Corpus Christi, U.S., and the Head and a Professor of the Department of Navigation and Positioning, Finnish Geodetic Institute, Finland. He has published two books: *Geospatial Computing in Mobile Devices and Ubiquitous Positioning* and *Mobile Location-Based Services in Smart Phones*. He has authored or co-authored more than 170 scientific papers and five book chapters. His research interests include smartphone positioning indoors/outdoors, context awareness, and satellite navigation. He was the President of the International Association of Chinese Professionals in Global Positioning Systems in 2008 and a Board Member of the Nordic Institute of Navigation from 2009 to 2012. He is the General Chair of the IEEE conferences, Ubiquitous Positioning, Indoor Navigation and Location-based Services, the Editor-in-Chief of the *Journal of Global Positioning Systems*, and an Associate Editor of the *Journal of Navigation*.

NASER EL-SHEIMY is currently a Professor at the Department of Geomatics Engineering, University of Calgary. He is the Tier-I Canada Research Chair in Geomatics Multi-Sensor Systems. He is a fellow of the Canadian Academy of Engineering and the U.S. Institute of Navigation. His research expertise includes geomatics multi-sensor systems, GPS/INS integration, and mobile mapping systems. He is also the Founder and CEO of Profound Positioning Inc. He published two books, six book chapters, and over 450 papers in academic journals, conference, and workshop proceedings, in which he has received over 30 national and international paper awards. He supervised and graduated over 60 master's and Ph.D. students. He was a recipient of many national and international awards, including the ASTech Leadership in Alberta Technology Award and the Association of Professional Engineers, Geologists, and Geophysicists of Alberta Educational Excellence Award.